High Voltage

Special Issue: Interface Charging Phenomena for Dielectric Materials

IET Journals
The Institution of Engineering and Technology

Gas–solid interface charge characterisation techniques for HVDC GIS/GIL insulators

eISSN 2397-7264
Received on 12th October 2019
Revised 28th December 2019
Accepted on 7th February 2020
E-First on 11th March 2020
doi: 10.1049/hve.2019.0289
www.ietdl.org

Lei Zhang[1], Chuanjie Lin[2], Chuanyang Li[3] ✉, Simone Vincenzo Suraci[3], Geng Chen[4], Uwe Riechert[5], Tohid Shahsavarian[6], Masayuki Hikita[7], Youping Tu[4], Zhousheng Zhang[1], Davide Fabiani[3], Jinliang He[2]

[1]*School of Electrical Engineering, Shanghai University of Electric Power, Changyang Road #2588, Shanghai, 200090, People's Republic of China*

[2]*State Key Laboratory of Power Systems, Department of Electrical Engineering, Tsinghua University, Beijing, 100084, People's Republic of China*

[3]*Department of Electrical, Electronic, and Information Engineering, 'Guglielmo Marconi', University of Bologna, Viale Risorgimento 2, Bologna, 40136, Italy*

[4]*Beijing Area Major Laboratory of High Voltage and Electromagnetic Compatibility, North China Electric Power University, Beijing 102206, People's Republic of China*

[5]*ABB Switzerland Ltd, High Voltage Products, Zurich, Switzerland*

[6]*Electrical Insulation Research Center, Institute of Materials Science, Electrical and Computer Engineering, University of Connecticut, Storrs, CT 06269, USA*

[7]*Kyushu Institute of Technology, Kitakyushu, Japan*

✉ *E-mail: lichuanyangsuper@163.com*

Abstract: Surface charge accumulation on the spacers is one of the key issues restraining the development of HVDC GIS/GIL. The precise measurement of surface charge properties provides the basis for further study of the surface charge transport mechanism as well as the charge-induced flashover mechanism under DC voltage. In this study, the authors discuss their perspective on the current status, development needs and potential developing orientation of surface charge characterisation techniques. Different surface potential measurement methods and charge inversion algorithms are reviewed regarding the previous studies and future research needs. Drawbacks and outlooks of surface charge measurement techniques are also discussed with the background of laboratory experiment results and on-site measurements. It is hopefully that this study can serve as a useful guide reference for researchers within the same research field. More importantly, it is authors' hope that this study can inspire some novel ideas for readers into developing of more accurate and scientific interface charge characterisation techniques.

1 Introduction

Charge accumulation on the surface of spacers inside HVDC GIS/GIL can modify the local electric field distribution, which potentially affects the safety of the HVDC system [1–5]. The investigation of the surface charge origin and charge-related surface breakdown phenomena therefore have been regarded as hot topics over the past few decades [6–13]. Surface charge accumulation can be due to the following aspects: gas phase ionisation, metal particles, cosmic radiation, charge transport inside volume [14–19], etc. As a basis of studying the surface charge behaviour, the surface potential of a charged surface must be measured, and an inversion algorithm is usually used to obtain the surface charge density distribution [20, 21]. However, due to the invisibility of surface charges as well as the difficulties in direct surface charge measurement, surface charge transport behaviours are still not clearly exposed and problems due to surface charge accumulation are still not well explained.

In our recently published paper, a field independent theory which clarifies the effects of bulk charging activity and surface net charge transport on surface potential measurement results of HVDC spacers, based on direct measurement of surface potential distribution, was put forward [22]. However, to further explore the surface charge-triggered surface breakdown mechanism, in particular the surface charge density and distribution as well as further estimations of the electric field distortion, still require more accurate measurement of surface charge properties.

In this paper, we discuss our perspective on the current status, development needs and potential developing orientation of surface charge measurement techniques. Different surface potential measurement methods and charge inversion algorithms are reviewed based on the combination of previous studies and future research needs. To make the content more universal and open to a wide range of readers in universities, research institutions and companies, we review and compare the methods and techniques with the combination of measurement cases obtained from previous studies. Differences between these research results are discussed and outlooks are provided for future development of novel surface charge measurement techniques.

2 Surface potential measurement methods

Accurate measurement of the surface potential is the basis for the calculation of surface charge density of GIS/GIL spacers [23]. This section mainly reviews the Lichtenberg figure method, the passive electrostatic probe and the active electrostatic probe methods. The analysis and discussion of the surface potential measurement are included along with measurement cases in previous research work. Since the Pockels effect method can only be used for the surface charge density measurement of transparent or translucent-insulating materials [24], it is not suitable for the insulators inside GIS/GIL and will not be included in this paper.

2.1 Lichtenberg figure method

The Lichtenberg figure method was firstly proposed by Lichtenberg in 1788, which has been continuously improved and used until the present [25]. The basic principle is to spray charged

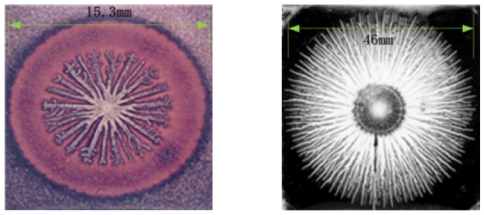

a b

Fig. 1 *Typical discharge figures recorded using the Lichtenberg figure method*

(a) Spray red Pb_3O_4 after applying −12 kV pulse voltage with the pulse width of 920 ns to the surface, ***(b)*** Spray white S after applying 12 kV pulse voltage with the pulse width of 450 ns to the surface [27]

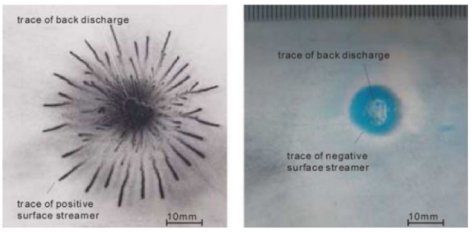

Fig. 2 *Lichtenberg figure of the surface charge using the toner after the PMMA was applied with 14 kV pulse voltage using a pair of hemispherical rod electrodes of 6 mm in diameter [28]*

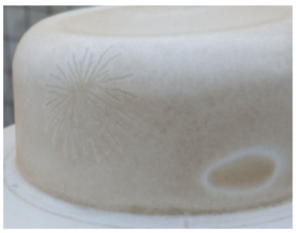

Fig. 3 *Lichtenberg figure of the surface charge by using uncharged dust profiles after the spacer was applied with −300 kV inside 0.5 MPa SF_6 for 30 min [15, 29, 30]*

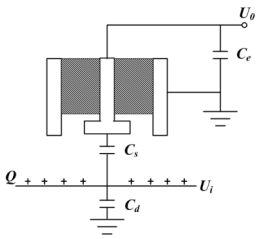

Fig. 4 *Schematic diagram of the original probe structure [34]*

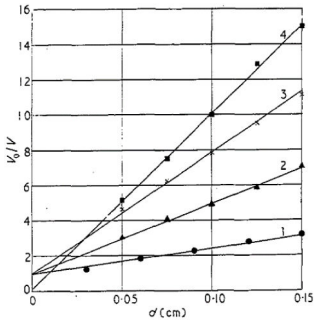

Fig. 5 *Variation of response with probe–surface separation for four dielectric specimens plotted as normalised inverse pulse amplitude against d: curve 1, NaCl (ε = 5.62, d_S = 0.4 cm); curve 2, KBr (ε = 4.78, d_S = 0.120 cm); curve 3, MgO (ε = 9.65, d_S = 0.139 cm); curve 4, polyethylene terephthalate (ε = 3, d_S = 0.003 cm) [34]*

dust with different colours onto the surface of charged insulating samples. The attachment of coloured dust on the insulation surface due to the electrostatic force can thereby reflect the surface charge distribution. Meanwhile, the polarity of the surface charge can also be obtained due to the polarity of the dust.

The commonly used dusts are the red Pb_3O_4 powders (density: 9.1 g/cm^3) with positive charges, and the yellow and white S powders (density: 2.36 g/cm^3) with negative charges [26]. Murooka *et al.* [27] studied the surface charge accumulation patterns of a smooth glass plate coated with a thin layer of SiR using the abovementioned dusts. The distribution of charges on the material surface was obtained by using the Pb_3O_4 and S powder as shown in Fig. 1.

Apart from Pb_3O_4 and S, researchers found that the toner (density: 3.8–4.7 g/cm^3) used in the printer is bright in colour, uniform in particles and self-charged. Therefore, it gradually becomes an optimal choice for the study of the Lichtenberg figure. Okabe *et al.* [28] obtained surface charge distribution on the sample after discharge treatment by using the toner and their results are shown in Fig. 2.

Recently, we found that the uncharged insulating particles (such as limestone dust filtered from dried mud) can also be used to draw a Lichtenberg figure as shown in Fig. 3 [15, 29, 30]. The mechanism is due to the directional movement caused by the polarisation of dust under the electric field created by surface-accumulated charges. Compared with the methods mentioned above, the density range of dust used in Fig. 3 is 0.7–1.5 g/cm^3, whose value is relatively small. By making dust mist suspended in air, the dust particles can be freely attached to the surface, which can thereby have less influence on the surface charge distribution and surface charge amount. Therefore, it can reflect the surface charge properties more accurately.

However, as is known that the Lichtenberg figure method cannot be a useful tool in quantitative analysis of surface charge density. Meanwhile, the physical process of the dust floating in air and its movement after attaching to the surface are very complicated, which involve the motion of particles under complex fields i.e. gravity field, electric field, interaction force of particles after polarisation, buoyancy of air, the interaction forces between the surface-adsorbed charge carriers and the possible covalent bond of surface radical trapped charges, etc. [30–33]. Therefore, it is very difficult to link the Lichtenberg figure results directly to the actual surface charge density distribution (or electric field distribution). In addition, the toner contains a lot of metal dust which makes the application of these powders not recommended since it is harmful to human health.

2.2 Passive electrostatic probe method

2.2.1 Concept and case study: The mechanism of the passive electrostatic probe method is electrostatic induction [30]. The equivalent circuit diagram is shown in Fig. 4. It mainly includes three parts: the sensing electrode, the grounding shell and the insulating support.

In 1967, Davies applied this method for the first time to measure the surface potential of NaCl, KBr, MgO and polyethylene terephthalate samples. He changed the distance d between the probe and the sample [34], and found that the responses with probe–surface separation for four dielectric specimens can be concluded as shown in Fig. 5. The points in the figure are measured values, and the line is the theoretical value calculated from the dielectric constant ε and thickness d_s of the sample. From the comparative analysis of measured values and theoretical values, his results showed that the measurement accuracy is closely related to the distance between the probe and the sample.

Based on previous research studies, in order to improve the accuracy of the probe, Wang *et al.* increased the creeping distance between the probe and the shield by increasing the distance between the insulating support and the probe [35]. This modification reduces the surface charge decay rate, and thereby improves the accuracy of the measurement results. The structure of the probe is shown in Fig. 6*a* [35, 38]. Meanwhile, a discontinuous

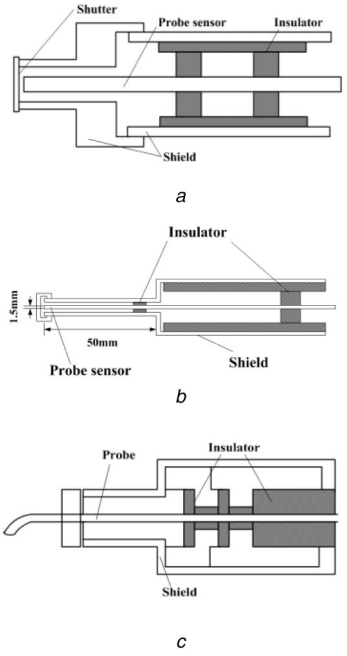

Fig. 6 *Schematic diagram of the improved probe structure by* ***(a)*** Wang [35], ***(b)*** Zhang [36], ***(c)*** Qi [37]

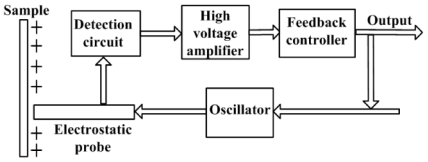

Fig. 7 *Schematic diagram of the measurement principle of active electrostatic probes*

Table 1 Main parameters of the active electrostatic probe measuring equipment

Model	Range	Accuracy, %	Dynamic response time
Trek341B	0 to ±20 kV	±0.1	<200 μs (1 kV)
Trek347	0 to ±3 kV	±0.05	<3 ms (1 kV)
TrekP0865	0 to ±10 kV	±0.1	<200 μs (1 kV)
Trek370	0 to ±3 kV	±0.05	<50 μs (1 kV)
Monroe244A	0 to ±3 kV	±0.1	<2.5 ms (1 kV)
Monroe279	0 to ±3 kV	±0.1	<2.5 ms (1 kV)

structure adopted for the insulating support leaves most of the space between the probe and the shield filled with air, which thereby reduces the capacitance of the probe. According to their experiment results, the improved probe calibration coefficient M is reduced from the original value of 6–7 to 0.86. As a result, the charge resolution of the capacitance probe increases [35, 38].

Based on the improved probe structure of Wang, Zhang *et al.* lengthened the front end of the capacitance probe, which further increased the creeping distance between the probe and the shield. The structure of the probe is shown in Fig. 6*b* [36]. Qi *et al.* adopted a hollow structure for the design of the insulating support, which can reduce the capacitance of the probe and increase the charge resolution of the probe. The structure of the probe is shown in Fig. 6*c* [37]. Meanwhile, in order to realise the multi-radial and multi-angle measurement of the surface charge, the shape of the probe is designed as a bevel probe, and the charge resolution of this probe is 0.02106 μC/(m^2 mV), and the spatial resolution is 6.3 mm^2 [37].

2.2.2 Advantages and shortcomings: Due to a simple structure and a high resolution, the passive electrostatic probe is usually used to detect surface charges on insulators with complex shapes [39]. However, it has the following disadvantages:

(i) The presence of the leakage current causes relatively higher error in the measurement result.

(ii) During the measurement, the grounded shielding can affect the detected original charge distribution of the surface. To the worst cases, gas breakdown is possible to be triggered in case of a surface being measured is deposited with a high surface charge density.

(iii) The potential feedback of the probe is sensitive to the distance between the detector and the insulator surface, which requires a precise control of the probe route.

2.3 Active electrostatic probe

2.3.1 Concept and case study: The active electrostatic probe overcomes the shortcomings of passive electrostatic probes and is therefore widely used [40–45]. It has been widely used by researchers in China, Japan, German, France, Switzerland, etc. [15–17, 46–55]. As an oscillating feedback capacitive probe, the Calvin probe is a typical representative of an active electrostatic probe [47]. The potential U_1 on the Calvin probe is set at first. Then, close the Calvin probe to the surface of the insulator to be tested. Assuming that the surface potential of the insulator facing the probe is U_2, the potential difference between the probe and the surface $\Delta U = U_1 - U_2$ is constant. When the distance between the probe and the surface of the insulator changes, the capacitance C_{ps} between the probe and the surface of the insulator will also changes under the action of the oscillator. Since the potential difference ΔU remains unchanged of C_{ps}, the amount of charges induced on the probe Q must be increased or decreased to accommodate the change of C_{ps} so that there is a corresponding current through the power supply circuit of the probe. According to the principle mentioned above, the probe is oscillated back and forth around a fixed position, and the potential on the probe is debugged according to the feedback current. When the probe voltage is at a certain voltage U_1, the probe current is always 0 and does not change with the probe position oscillation. The probe potential U_1 is equal to the measured surface potential U_2. The principle mentioned above is shown in Fig. 7.

At present, the active electrostatic probe measuring equipment on the market mainly comes from Trek and Monroe. The main parameters of their products are shown in Table 1.

2.3.2 Advantages and shortcomings: Comparing with the passive electrostatic probe, the output of the active electrostatic probe is not sensitive to the measurement distance within a certain range. When the distance between the probe and the dielectric surface is controlled within 3 mm, the potential error of the probe output can be controlled within 2% [56–59]. Meanwhile, the potential of the probe is close to the real potential of the surface measured, which does not affect the surface potential and will not excite a surface discharge. However, the disadvantage of this type of probe is that the longer response time of the probe limits the possibility of real-time measurement [57, 58].

3 Surface charge inversion algorithm

The surface charge inversion algorithm is used to transform the surface potential into a surface charge density. This section reviews the evolution of the inversion algorithm over the past 50 years as shown in Fig. 8.

3.1 The linear algorithm (TLA)

In 1967, Davies found that there was a linear relationship between surface potential V_m measured by electrostatic probes and surface charge density σ [34], which is $\sigma = MV_m$; M is the linear coefficient, determined by the structural parameters of the electrostatic probe and measurement system. The overall structure of the electrostatic probe measurement system and the equivalent circuit diagram is shown in Fig. 9.

In the figure, C_m is the sum of the inlet capacitance of the electrostatic probe and C_p is the capacitance due to the air gap

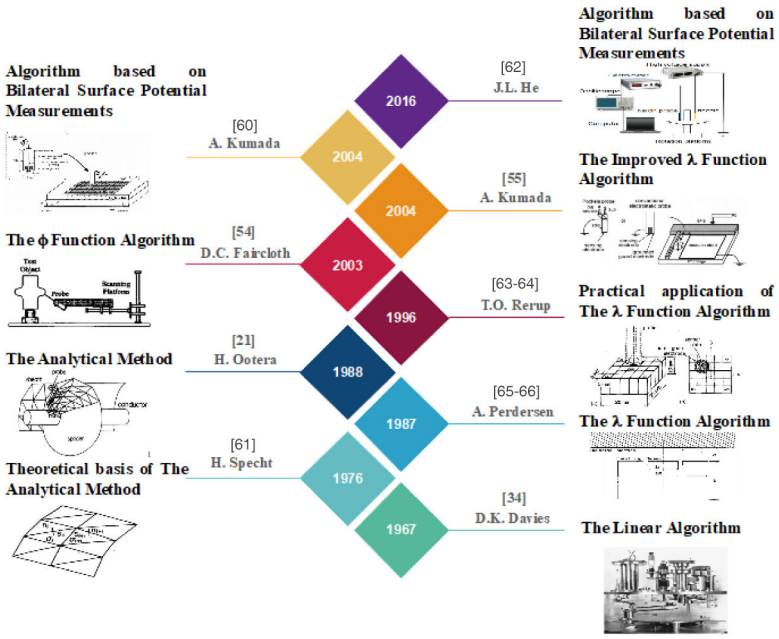

Fig. 8 *Development of inverse algorithms over the past 50 years*

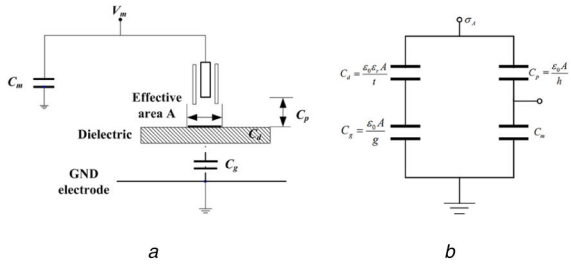

Fig. 9 *Structure and equivalent circuit of electrostatic probe measurement system*

(a) Structure diagram of electrostatic probe measurement system, ***(b)*** Related equivalent circuit diagram [67]

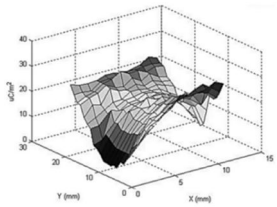

Fig. 10 *Surface charge density distribution of PTFE samples after applying 30 kV impulse voltage (0.4/2.5 μs) [68]*

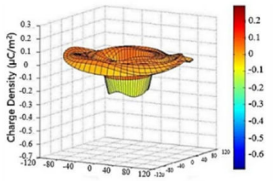

Fig. 11 *Surface charge density distribution of 220 kV GIS disc insulator model after applying 80 kV AC voltage for 2 h [69]*

between the electrostatic probe and the dielectric surface; C_d is the dielectric capacitance; C_g is the capacitance due to the air gap between the dielectric and ground electrode. The assumption for the C_p, C_d and C_g formulas is an approximately uniform electric field formed between the probe, the sample and the ground electrode [67].

From Fig. 9*b*, the relationship between the output potential of the probe and the surface charge density in the effective area can be deduced using the following formula:

$$V_m = \frac{C_p}{C_p + C_m} \frac{A\sigma_A}{C_d C_g/(C_d + C_g) + C_p C_m/(C_p + C_m)} \quad (1)$$

where V_m is the output voltage of the electrostatic probe, A is the effective area and σ_A is the surface charge density on the effective area. If the gap distance between the dielectric surface and the ground electrode is very close to 0, and $C_m \gg C_d$, then (2) can be deduced by (1):

$$V_m = \frac{A\sigma_A}{C_m(1 + \varepsilon_r h/t)} \quad (2)$$

where ε_r is the relative dielectric constant of the dielectric; h is the vertical distance from the surface of the probe to the surface of the dielectric and t is the thickness of the dielectric. Then the surface charge density on the dielectric can be calculated using the following formula:

$$\sigma_A = V_m \frac{C_m(1 + \varepsilon_r h/t)}{A} \quad (3)$$

This algorithm was used by many scholars to study the insulation sheet with a certain thickness. Zhang *et al.* [68] used TLA to study the effect of surface charge density on the surface flashover voltage. They used a rectangular Polytetrafluorethylene (PTFE) with a length of 30 mm and a width of 15 mm. The distance between the needle electrode and the surface of the sample is 10 mm. After applying 30 kV impulse voltage (0.4/2.5 μs), the surface charge density distribution of the sample is as shown in Fig. 10.

Li *et al.* [69] used TLA to study the surface charge accumulation of the 220 kV GIS disc model insulator under AC voltage. After applying 80 kV AC voltage for 2 h to the disc insulator model, the observed surface charge density distribution is as shown in Fig. 11.

However, as mentioned above, TLA is established under an approximately uniform electric field. Otherwise, a large error to the measurement results would be introduced. Meanwhile, the algorithm requires the probe to be as close as possible to the dielectric, and the thickness of the sample must be uniform and thin enough (usually <5 mm) [70, 71]. In addition, the leakage current of the measuring system could cause errors due to the changing of the capacitance during the movement of the probe. These defects reduce the accuracy of TLA and in some way limit its application in samples with higher thickness dimensions such as insulators inside GIL/GIS.

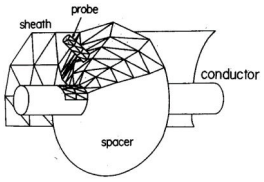

Fig. 12 *Cone-type spacer and part of coaxial cylinders and their divided surfaces [21]*

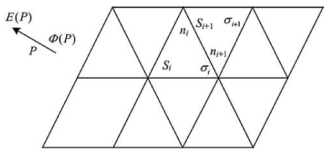

Fig. 13 *Schematic diagram of dielectric surface area division [67]*

3.2 The analytical method (TAM)

Due to the limitations of TLA, new inversion algorithms are in need urgently with the increasingly usage of post type insulator and spacers in gas-insulated devices [61, 65, 66, 72]. In 1976, Specht [63] proposed that the output potential of the probe is not only affected by the surface charge in the effective area, but should be expressed as a superposition of all surface charges. If the measured surface is divided into N finite cells, the potential at the measurement point i can be expressed as (4):

$$V_{\mathrm{m}}(i) = \sum_{j=1}^{N} h(i,j)\sigma(i) \tag{4}$$

where $h(i, j)$ is the output of the probe at point i generated by a unit charge at element j.

In 1988, Ootera *et al.* firstly applied this idea in their surface charge measurement on a cone-type spacer in GIS, and proposed TAM from the basic formula of electromagnetic field [21]. The meshing of the cone-type spacer and part of coaxial cylinders is shown in Fig. 12.

TAM mainly uses the finite element method to mesh the insulation surface according to the triangular element as shown in Fig. 13.

Due to the electrostatic field conditions, (5) and (6) can be obtained from Maxwell's equations:

$$\nabla \cdot D = \rho \tag{5}$$

$$\nabla \times E = 0 \tag{6}$$

where D is the electric flux density; ρ is the bulk charge density and E is the electric field. Formula (7) shows the relationship between electric field E and flux density D:

$$D = \varepsilon_0 E + p \tag{7}$$

where p represents the polarisation effect of the dielectric and ε_0 represents the relative dielectric constant in vacuum. Formula (8) can be obtained by combining (5) and (7):

$$\varepsilon_0 \nabla \cdot E = \rho - \nabla \cdot p = \rho' \tag{8}$$

where ρ' is the apparent bulk charge density. From the basic formula of electromagnetic field, the electric potential and electric field at the measurement point P can be obtained as follows:

$$\Phi(P) = \frac{1}{4\pi\varepsilon_0}\int \frac{\rho'}{r}\,\mathrm{d}V \tag{9}$$

$$E(P) = \frac{1}{4\pi\varepsilon_0}\int \frac{\boldsymbol{r}\rho'}{r^3}\,\mathrm{d}V \tag{10}$$

Assuming that there is no charge in the internal space of the dielectric, the charge exists only on the surface of the dielectric. The bulk charge in (9) and (10) can be converted into surface charge:

$$\Phi(P) = \frac{1}{4\pi\varepsilon_0}\int \frac{\sigma'}{r}\,\mathrm{d}S \tag{11}$$

$$E(P) = \frac{1}{4\pi\varepsilon_0}\int \frac{\boldsymbol{r}\sigma'}{r^3}\,\mathrm{d}S \tag{12}$$

Assuming that the surface charge is evenly distributed in the divided triangular region, the potential and electric field in each triangular region can be obtained using (13) and (14):

$$\Phi(P) = \frac{1}{4\pi\varepsilon_0}\sum_{i=1}^{n}\sigma_i'\int_{S_i}\frac{1}{r}\,\mathrm{d}S \tag{13}$$

$$E(P) = \frac{1}{4\pi\varepsilon_0}\sum_{i=1}^{n}\sigma_i'\int_{S_i}\frac{\boldsymbol{r}}{r^3}\,\mathrm{d}S \tag{14}$$

where σ_i' is the apparent surface charge density at the ith area; S_i is the ith small area and r is the distance from the centroid of area i to the measurement point. The interface boundary conditions of the dielectric are given as (15):

$$(\varepsilon_2 E_2 - \varepsilon_1 E_1)\cdot \boldsymbol{n} = \sigma \tag{15}$$

where ε_2 and E_2 are the dielectric constant and electric field strength on the outer side of the insulator (i.e. the gas side), respectively; ε_1 and E_1 are the dielectric constant and electric field strength inside the dielectric, respectively and σ is the actual surface charge density. Then the electric potential at any point j in the finite element $1 \sim n$ can be obtained as follows:

$$\Phi_j = \frac{1}{4\pi\varepsilon_0}\sum_{i=1}^{n}\sigma_i'\int_{S_i}\frac{1}{r_{ij}}\,\mathrm{d}S \tag{16}$$

$$(\varepsilon_2 - \varepsilon_1)\frac{1}{4\pi\varepsilon_0}\sum_{i=1}^{n}\sigma_i'\int_{S_i}\frac{\boldsymbol{r}_{ij}\boldsymbol{n}_j}{r_{ij}^3}\,\mathrm{d}S = \sigma_j \tag{17}$$

where $\boldsymbol{r}_{ij}$ is the distance between the centroid of region i and region j; $\boldsymbol{n}_j$ is the normal vector perpendicular to surface j and σ_j is the actual surface charge density of the region j. Formula (18) is the matrix form of (16) and (17):

$$\begin{bmatrix} P_{11} & P_{12} & \cdots & P_{1n} \\ P_{21} & P_{22} & \cdots & P_{2n} \\ \vdots & \vdots & \ddots & \vdots \\ P_{m1} & P_{m2} & \cdots & P_{mn} \\ F_{m+1,1} & F_{m+1,2} & \cdots & F_{m+1,n} \\ \vdots & \vdots & \ddots & \vdots \\ F_{n1} & F_{n2} & \cdots & F_{nn} \end{bmatrix} \begin{bmatrix} \sigma'_1 \\ \sigma'_2 \\ \vdots \\ \sigma'_m \\ \sigma'_{m+1} \\ \vdots \\ \sigma'_n \end{bmatrix} = \begin{bmatrix} \Phi_1 \\ \Phi_2 \\ \vdots \\ \Phi_m \\ \sigma_{m+1} \\ \vdots \\ \sigma_n \end{bmatrix} \tag{18}$$

In (18), the number $1 \sim m$ is the area of the conductor surface, and the number $(m+1) \sim n$ is the area of the insulator surface, where

$$P_{ij} = \frac{1}{4\pi\varepsilon_0}\int_{S_i}\frac{1}{r_{ij}}\,\mathrm{d}S \tag{19}$$

$$F_{ij} = (\varepsilon_2 - \varepsilon_1)\frac{1}{4\pi\varepsilon_0}\int_{S_i}\frac{\boldsymbol{r}_{ij}\boldsymbol{n}_j}{r_{ij}^3}\,\mathrm{d}S \tag{20}$$

Defining the matrix $\boldsymbol{A} = (a_{ij})$ is the inverse of the coefficient matrix in (18):

$$A = \begin{bmatrix} P_{11} & P_{12} & \cdots & P_{1n} \\ P_{21} & P_{22} & \cdots & P_{2n} \\ \vdots & \vdots & \ddots & \vdots \\ P_{m1} & P_{m2} & \cdots & P_{mn} \\ F_{m+1,1} & F_{m+1,2} & \cdots & F_{m+1,n} \\ \vdots & \vdots & \ddots & \vdots \\ F_{n1} & F_{n2} & \cdots & F_{nn} \end{bmatrix}^{-1} \quad (21)$$

The apparent charge density can be obtained as follows:

$$\sigma_i' = \sum_{j=1}^{m} a_{ij}\Phi_j + \sum_{k=m+1}^{n} a_{ik}\sigma_k \quad (22)$$

Formula (23) can be obtained by combining (16) and (19):

$$\Phi_j = \frac{1}{4\pi\varepsilon_0}\sum_{i=1}^{n}\sigma'_i\int_{S_i}\frac{1}{r_{ij}}\mathrm{d}S = \sum_{i=1}^{n}P_{ij}\sigma'_i \quad (23)$$

Combining (22) and (23), the relationship between the potential of the point x and the actual charge density is obtained using (24):

$$\Phi_x = \sum_{i=1}^{n}P_{ix}\left(\sum_{j=1}^{m}a_{ij}\Phi_j + \sum_{k=m+1}^{n}a_{ik}\sigma_k\right) \quad (24)$$

Thus, the actual surface charge density can be calculated by using a computer.

In order to verify the effectiveness of the algorithm, Ootera *et al.* [21] applied 500 kV DC voltage to the disc insulator for 30 min, comparing the charge density distribution obtained by using the Lichtenberg figure method and TAM. The experimental results are shown in Fig. 14. The results showed that the profile of the surface charge distribution obtained by two methods is consistent. TAM is the first algorithm that considers all the charge contributions, and is the first algorithm that can be applied to large-sized insulators. Most of the algorithms introduced later are based on this algorithm.

Zhang *et al.* applied this algorithm to measure the surface charge density of the spacer model in GIS as shown in Fig. 15. DC voltage (−40 kV) was applied for 300 min at 0.1 MPa. The surface charge density distribution is shown in Fig. 16. During their measurement, they introduced artificial error to the output voltage of the probe at −40 kV. They also proposed that 2% error in the potential output from the probe would result in an error of calculated charge density up to 14%.

In our previous research [67], we used an electrostatic probe to measure the surface potential distribution after applying −3 kV DC voltage to the disc insulator for 1 min. The distribution of surface charge density on the insulator after discharge was calculated using TAM and TLA, respectively. The results are shown in Fig. 17. We compared the differences of the results between TAM and TLA.

From Fig. 17, it can be observed that the discharge area obtained by TLA and TAM is very similar, which can be taken as a mutual verification. Since the electrode discharge result in negative charges accumulated in the local area of the disc insulator, the other non-treated areas should contain a relatively low amount of charge. However, in the surface charge density distribution calculated by TLA, the surface area outside the negative corona region shows a large amount of relatively uniform positive charge density distribution, which deviates from the true value. In the charge density distribution calculated by TAM, the charge amount in most regions is very small. There is positive charge with a slightly higher amplitude near the corona treatment region, which verifies that TAM is more accurate than TLA.

From the above analysis, the inversion algorithm based on TAM mainly has the following problems:

(i) The output errors caused by the probe movement are difficult to be avoided.

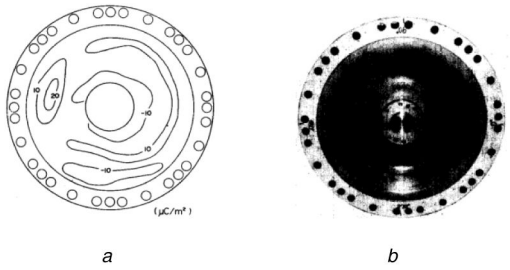

a *b*

Fig. 14 *Ootera's verification experiment of TAM*
(a) Charge density distribution obtained by TAM, ***(b)*** Lichtenberg figure [21]

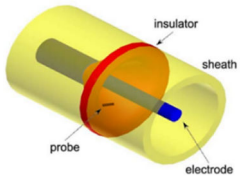

Fig. 15 *Disc model insulator [56]*

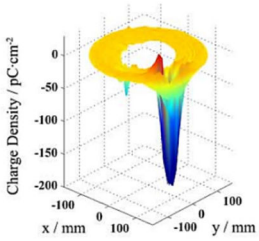

Fig. 16 *Surface charge density distribution of a disc insulator model after applying −40 kV DC voltage for 300 min [56]*

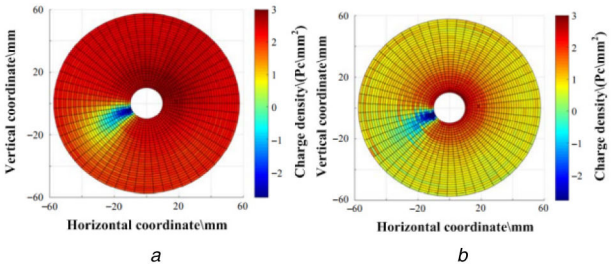

a *b*

Fig. 17 *Surface charge density distribution of insulator after applying −3 kV DC voltage for 1 min*
(a) Linear algorithm, ***(b)*** Analytical method [67]

(ii) Due to the complexity of TAM, the contribution of the surface charge to the output of the probe cannot be calculated completely accurate by computers.

(iii) The algorithm includes two inversions of the large matrix, when the number of meshes is too large, it would diverge.

3.3 λ function algorithm (λFA) and φ function algorithm (φFA)

In 1984, Perdersen *et al.* proposed that the charge induced on the electrostatic probe is the basic charge amount recorded by the probe. They verified a complex non-linear relationship between the amount of charges induced on the electrostatic probe and the parameters of the probe. The parameters of the probe include the capacitance, the size and the vertical distance from the probe to the dielectric surface [64, 73]. In 1987, based on their previous assumption, they further proposed the λFA. In λFA, the unit charge on the finite element of the dielectric surface dq can generate the charges dQ_i induced on the surface of the probe, which can be expressed by the following formula:

$$\mathrm{d}q = -\lambda\mathrm{d}Q \quad (25)$$

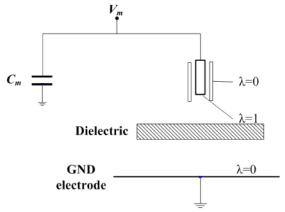

Fig. 18 *Schematic diagram of boundary conditions*

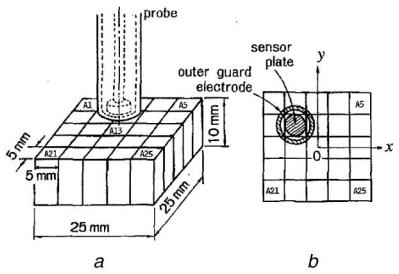

Fig. 19 *Schematic diagram of system grid division [64]*
(a) 3D sketch, ***(b)*** Plan view

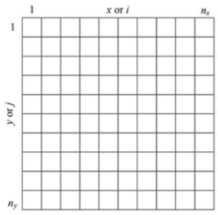

Fig. 20 *Schematic diagram of dielectric surface area division by λFA [67]*

where λ a solution of the general Laplace equation for the complete system geometry. Assuming that the relative dielectric constant of the dielectric is independent of the electric field strength and there is no bulk charge inside the dielectric, the above (25) can be written as follows:

$$q = -\int\int_{A_0} \lambda\sigma \mathrm{d}A \tag{26}$$

where A_0 is the area of the entire dielectric surface region; σ is the surface charge density of the corresponding micro-element dA and λ is the solution of the Laplace equation of the geometry of the measurement system as follows:

$$\nabla(\varepsilon \cdot \nabla\lambda) = 0 \tag{27}$$

The boundary conditions at the interface of the dielectric are represented by (28); and $\lambda = 1$ at the probe sensor; $\lambda = 0$ at other parts of the probe and electrode parts. The boundary conditions for the device are shown in Fig. 18:

$$\varepsilon_+\left(\frac{\partial\lambda}{\partial n}\right)_+ = \varepsilon_-\left(\frac{\partial\lambda}{\partial n}\right)_- \tag{28}$$

where '+' and '−' are parameters representing the upper and lower sides of the interface.

In 1996, Rerup *et al.* [74, 75] discretised the surface area and updated the λ function as:

$$\boldsymbol{q} = \boldsymbol{\Lambda\sigma} \tag{29}$$

where $\boldsymbol{q}$ is the vector composed of the quantity of charges induced by the probe at different positions; $\boldsymbol{\sigma}$ is the vector composed of the actual surface charge density of different regions and $\boldsymbol{\Lambda}$ is a parameter matrix composed of λ at different regions. The value of $\boldsymbol{\Lambda}$ depends only on the geometry of the device and the sample.

Based on the experiment of Yashima [71], Rerup *et al.* used a rectangular parallelepiped sample (25 × 25 mm^2 and a thickness of 10 mm) to verify the feasibility of the algorithm. The upper surface was divided by 5 × 5 mm^2 as shown in Fig. 19.

Different locations of the probe above the surface of the dielectric result in different measurement results. For example, when the probe is at the position of A13 (as shown in Fig. 19), the charge induced on the probe obtained by λFA is as follows:

$$q_{13} = \begin{bmatrix} 3.3 & 5.0 & 6.6 & 0.4 & 2.8 \\ 5.1 & 11.7 & 28.6 & 1.5 & 5.0 \\ 7.0 & 28.6 & 131.1 & 3.3 & 5.9 \\ 2.6 & 11.5 & 32.8 & 1.4 & 4.6 \\ 1.1 & 4.8 & 6.7 & 0.9 & 3.1 \end{bmatrix} \tag{30}$$

Each element in the above matrix represents the contribution of the surface charge on the surface region A1 to A25 to the charge induced on the probe:

$$q_{13} = \sum_{j=1}^{25} p_{13,j} = 315.4 \tag{31}$$

It can be found that the charge induced on the probe $q_{13,13}$ only accounts for 41.57% of the total amount of the charge induced, and the contribution of all boundary regions accounts for 20.58% of the total amount of the charge induced. In the application of λFA, the three-dimensional (3D) model is simplified into the two-dimensional (2D) model for simplifying calculation. Although the amount of calculated value is reduced, the errors generated on the boundary have become larger. Meanwhile, due to the lack of 3D finite element software, they used 2D finite element software to determine the function λ. However, in the actual case, the reduction of the incompletely symmetric 3D sample into a 2D model could lead to errors in the boundary.

To solve this problem in the boundaries, based on λFA, Faircloth [57] *et al.*, in 2003, defined the voltage values V measured on the probe using the following formula:

$$V = \sum v = \sum \phi\sigma \tag{32}$$

where the total probe voltage V is the sum of the contributions v from all the elements of surface charges. Each element has a different associated φ value depending on its distance from the probe. For the probe in one particular position, the probe response function consists of the φ values for all the elements on the surface. For example, a square area was divided into n_x columns and n_y rows as shown in Fig. 20. The coordinates of the small area are represented by (x, y) and the coordinates of the probe are represented by (i, j). Then the φ function can be obtained as follows:

$$V_{ij} = \sum_{y=1}^{n_y}\left[\sum_{x=1}^{n_x}\phi_{ij}(x,y)\sigma_{xy}\right] \tag{33}$$

where $\varphi_{ij}(x, y)$ is a parameterised form of the φ function, it corresponds to the contribution coefficient of the charge density at position (x, y) for the probe at position (i, j) and σ_{xy} is the charge density on the surface element at position (x, y). Formula (34) is the matrix form of (33): (see (34)) . Formula (34) is abbreviated as follows:

$$\boldsymbol{V} = \boldsymbol{\sigma\Phi} \tag{35}$$

Then the surface charge density can be obtained using (36):

$$\boldsymbol{\sigma} = \boldsymbol{V\Phi}^{-1} \tag{36}$$

The matrix $\boldsymbol{\Phi}$ is found by moving a unit charge over the dielectric surface. The proximity of the probe to the ground plane is then varied and the matrix $\boldsymbol{\Phi}$ is calculated using mathematical software.

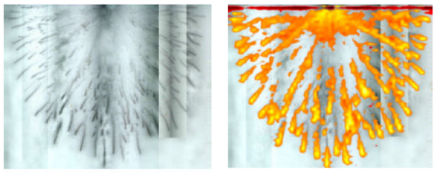

a b

Fig. 21 *Verification experiment of φFA*
(a) Lichtenberg figure, ***(b)*** Combined Lichtenberg figure and charged region [57]

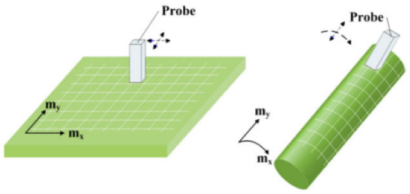

Fig. 22 *Translation invariant system*

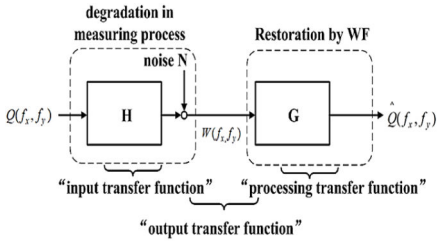

Fig. 23 *Structure diagram of the measurement system [77]*

Faircloth *et al.* [57] used a 3D electrostatic field solver to remove the error caused by the boundary condition which occurs when the 3D model is simplified into a 2D model. This solution introduces the φFA with higher precision than λFA. However, φFA considers the movement of the probe, and the dimension of the calculation is greatly changed from the (n_x, n_y) of λFA to the ($n_x n_y$, $n_x n_y$), which makes the computation time-consuming.

Meanwhile, Faircloth verified the effectiveness of the algorithm by using Lichtenberg figure simultaneously, as shown in Fig. 21. It was found that the profile of the charge density distribution was basically consistent with the profile in the Lichtenberg figure.

From the above-mentioned analysis, we can draw a conclusion that the λFA has a higher accuracy than TLA, but it produces a larger error at the boundary in the process of simplifying the 3D model to the 2D model. φFA further improves the accuracy compared with λFA, at the expense of increasing calculation time.

3.4 Improved λ function algorithm (IλFA)

Since λFA takes into account the effect of the entire dielectric surface on the output of the probe, the complexity of the algorithm is greatly increased. This in turn would result in a limited number of measurement points in the previous study (limited within 300 points) [76, 77]. In 2004, Kumada *et al.* proposed the improved λFA based on the Fourier transform algorithm [58]. This algorithm is mainly used for translation-invariant systems such as flat plates with a large area and a long cylindrical tube, as shown in Fig. 22. This algorithm greatly reduces the influence of noise on the measurement results by using the Wiener filter. In their experiments, the number of measurement points can be up to 250,000.

For the translation invariant system, the surface charge density can be obtained using (37):

$$\sigma_{N\times 1} = H^{-1}_{N\times N} V_{N\times 1} \tag{37}$$

However, the inversion of such large matrices is unstable [78]. To solve this problem, (37) is expressed as a form of double convolution as follows:

$$V(m_x, m_y) = \sum_{k_x=-\infty}^{\infty} \sum_{k_y=-\infty}^{\infty} h(m_x - k_x, m_y - k_y)\sigma(k_x, k_y) + n \quad (m_x, m_y) \tag{38}$$

where $\sigma(k_x, k_y)$ represents the surface charge density at position (k_x, k_y); $h(m_x - k_x, m_y - k_y)$ is the potential at position (m_x, m_y) generated by the unit charge at position (k_x, k_y) and $n(m_x, m_y)$ represents the noise in the experiment. Formula (39) can be obtained by performing a 2D Fourier transform on (38):

$$\boldsymbol{V}(f_x, f_y) = \boldsymbol{H}(f_x, f_y)\boldsymbol{\sigma}(f_x, f_y) + \boldsymbol{N}(f_x, f_y) \tag{39}$$

where $\boldsymbol{V}(f_x, f_y)$, $\boldsymbol{H}(f_x, f_y)$, $\boldsymbol{\sigma}(f_x, f_y)$ and $\boldsymbol{N}(f_x, f_y)$ are the expression of $V(m_x, m_y)$, $h(m_x - k_x, m_y - k_y)$, $\sigma(k_x, k_y)$ and $n(m_x, m_y)$ in the frequency domain.

The Wiener filter is based on the Tikhonov regularisation principle and the minimum squared error between the real output and the desired output as shown in (40):

$$\min : \| H\sigma - V \|^2 + \| \alpha\sigma \|^2 \tag{40}$$

where α is a regularisation parameter.

The estimated charge density $\hat{\boldsymbol{\sigma}}$ after reconstruction by the Wiener filter can be obtained using (41):

$$\hat{\boldsymbol{\sigma}}(f_x, f_y) = \frac{\boldsymbol{H}^*(f_x, f_y)}{|\boldsymbol{H}(f_x, f_y)|^2 + C}\boldsymbol{V}(f_x, f_y) \tag{41}$$

where C is the filter coefficient and is constant and $\boldsymbol{H}^*$ is the conjugate matrix of $\boldsymbol{H}$. The deterioration of the signal via measurement and the restoration of the signal can be expressed as shown in Fig. 23.

Meanwhile, Zhang *et al.* [23] verified the effectiveness of the algorithm by numerical simulation method. First, the initial charge density distribution was set. The resulting surface potential is calculated by electrostatic field computation. After adding 0.1 and 0.5% Gaussian noise to the surface potential, respectively, the estimated charge density distribution was calculated using (41). The result is shown in Fig. 24.

Based on the results of numerical simulation, it can be seen that the charge density distribution obtained by the Wiener filter is similar to the initial charge density distribution, which verifies the effectiveness of the algorithm in noise suppression. By using IλFA, the charge density distribution on the cone-type insulator was measured after applying −20 kV DC voltage for 6 h under atmospheric air. The result is shown in Fig. 25.

Zhang *et al.* [79] applied this algorithm to measure the surface charge density of the spacer model in GIL. For spacers coated with SiC/epoxy coatings of different SiC mass fractions, surface charge distributions under 0.1 MPa 20% SF_6/N_2 mixtures under DC voltage are presented in Fig. 26.

$$\begin{bmatrix} V_{11} & V_{12} & \cdots & V_{n_x n_y} \end{bmatrix} = \begin{bmatrix} \sigma_{11} & \sigma_{12} & \cdots & \sigma_{n_x n_y} \end{bmatrix} \times \begin{bmatrix} \phi_{11}(1,1) & \phi_{12}(1,1) & \cdots & \phi_{n_x n_y}(1,1) \\ \phi_{11}(1,2) & \phi_{12}(1,2) & \cdots & \phi_{n_x n_y}(1,2) \\ \vdots & \vdots & \ddots & \vdots \\ \phi_{11}(n_x, n_y) & \phi_{12}(n_x, n_y) & \cdots & \phi_{n_x n_y}(n_x, n_y) \end{bmatrix} \tag{34}$$

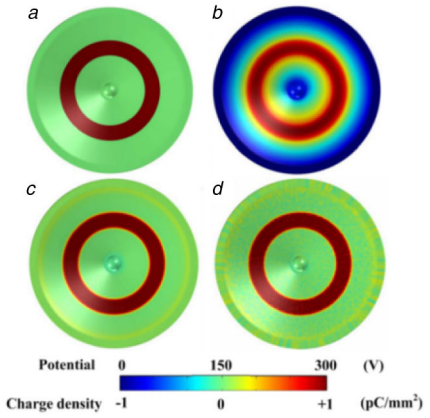

Fig. 24 *Numerical simulation*
(a) Original assumed surface charge distribution, ***(b)*** Calculated surface potential distribution, ***(c)*** Estimated surface charge distribution when 0.1% Gaussian noise is superimposed to the surface potential, ***(d)*** Estimated surface charge distribution when 0.5% Gaussian noise is superimposed to the surface potential [23]

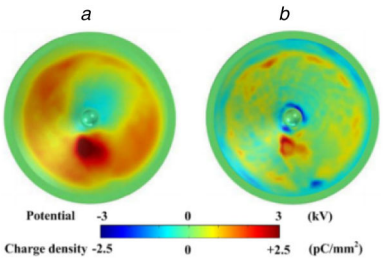

Fig. 25 *Charge density distribution on a cone-type insulator after applying −20 kV DC voltage for 6 h under atmospheric air*
(a) Measured surface potential, ***(b)*** Estimated surface charge [23]

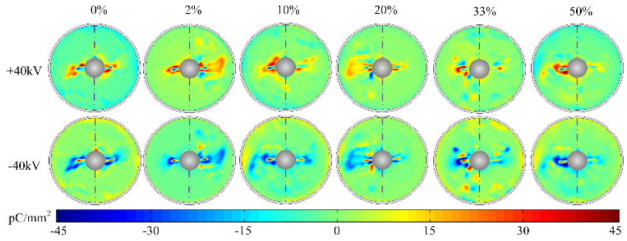

Fig. 26 *Surface charge distribution under 0.1 MPa 20% SF_6/N_2 mixtures on different SiC/epoxy-coated spacers after 10 min DC application [79]*

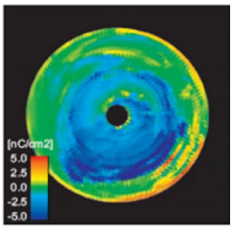

Fig. 27 *Charge density distribution on a disc insulator after applying −10 kV DC voltage for 19 h [82]*

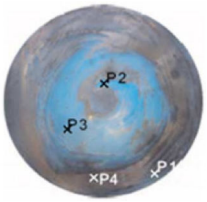

Fig. 28 *Lichtenberg figure on a disc insulator after applying −10 kV DC voltage for 19 h [28]*

Since the geometry of the probe affects the value of $\boldsymbol{H}$ [80, 81], Kumada *et al.* used IλFA to quantitatively discuss the influence of the geometry of the probe on the spatial resolution. They introduced the optimal choice of probe geometry in several typical measurements [74]. The accuracy of the algorithm can be quantified by the signal-to-noise ratio (SNR) and the peak-mean square error (PMSE). When IλFA is used with the Wiener filter, the PMSE is <7%. However, the PMSE of the simple inverse calculation without the Wiener filter exceeds 30%. It can be found that the accuracy of IλFA is greatly improved compared with the simple inversion algorithm. With their experience, Kumada *et al.* [82] applied the algorithm to the measurement of the surface charge density of a truncated cone spacer. After applying −10 kV DC voltage of to the insulator for 19 h, the obtained results are shown in Fig. 27.

Based on the experiments conducted by Kumada, Okabe *et al.* [28] verified the effectiveness of the algorithm by the Lichtenberg figure (Fig. 28), whose results are consistent well with charge calculation results.

The IλFA solves the equation of surface charge in the frequency domain, which avoids the inversion of the matrix. This algorithm effectively suppresses the influence of noise in the measurement, which greatly improves the calculation. However, this algorithm can only be used for the translation invariant system, which somehow may limit its application.

3.5 Inversion algorithm based on bilateral surface potential

In the algorithm described above, only the surface potential of one side has been considered. Since some of the objects to be tested are thin, the surface charge on the other side is bound to affect the result of measurement. Even if for a sample with a certain thickness, the charge on the opposite side can have a significant effect on the charge on the measured side [60]. Winter and Kindersberger used two electrostatic probes to measure the charge distribution on both sides of the insulator [62, 83, 84], but they did not consider the effect of surface charge on both sides of the insulator on the output of the probe.

In 2004, Kumada *et al.* proposed an inversion algorithm based on bilateral surface potential measurements, which considers the effect of surface charge on both sides of the insulator on the output of the probe [85]. They believed that the charge induced on the probe is the result of all the charges that accumulated on the upper and lower surfaces of the dielectric. Formula (42) can be obtained from (38):

$$V(m_x, m_y) = \sum_{k_x=-\infty}^{\infty}\sum_{k_y=-\infty}^{\infty} h_\alpha(m_x - k_x, m_y - k_y) \times \sigma_\alpha(k_x, k_y) + \sum_{k_x=-\infty}^{\infty}\sum_{k_y=-\infty}^{\infty} h_\beta(m_x - k_x, m_y - k_y) \times \sigma_\beta(k_x, k_y) \quad (42)$$

where $\sigma_\alpha(k_x, k_y)$ and $\sigma_\beta(k_x, k_y)$ are the surface charge density at the upper and lower surfaces of the insulator at position (k_x, k_y), respectively; $h_\alpha(m_x - k_x, m_y - k_y)$ and $h_\beta(m_x - k_x, m_y - k_y)$ are the potential at the upper and lower surfaces (m_x, m_y) generated by the unit charge at (k_x, k_y), respectively. After that, performing the same Fourier transform and filtering as in Section 3.4, the following formula is obtained:

$$\hat{\boldsymbol{\sigma}} = [G]\boldsymbol{V} \quad (43)$$

where

$$\hat{\boldsymbol{\sigma}} = \begin{pmatrix}\hat{\sigma}_\alpha \\ \hat{\sigma}_\beta\end{pmatrix}, \quad [G] = \left([H]^{\mathrm{T}}[H] + \gamma[I]\right)^{-1}[H]^{\mathrm{T}} \quad (44)$$

Using inverse Fourier transform, the surface charge density σ_α and σ_β can be obtained.

Okabe verified the effectiveness of the algorithm by numerical simulation method [28]. The measurement of dual-layer charges

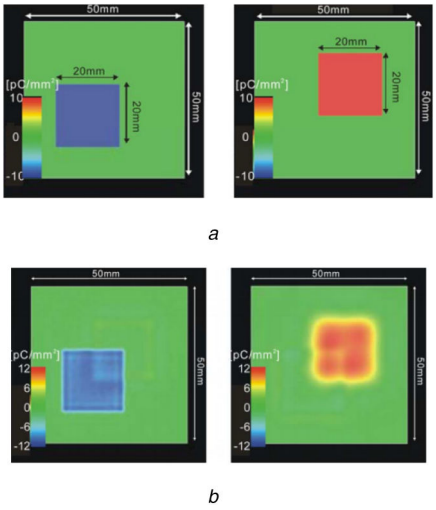

Fig. 29 *Verifying the accuracy of the inversion algorithm using the numerical simulation method*

(a) Original assumed charge distribution (left: upper surface σ_α; right: lower surface σ_β), ***(b)*** Estimated charge distribution based on bilateral surface potential measurements [28] (left: upper surface σ_α ($g = 2$ mm, $d = 2$ mm); right: lower surface σ_β ($g = 2$ mm, $d = 5$ mm))

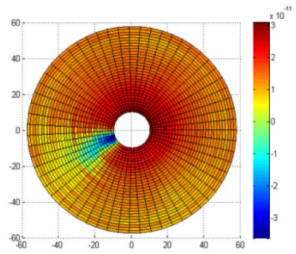

Fig. 30 *Charge density distribution on convex surface after applying −3 kV DC voltage for 30 min by the unmodified algorithm [86]*

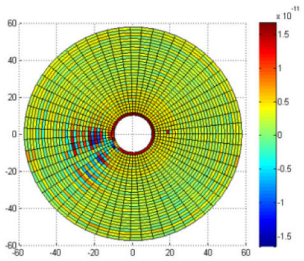

Fig. 31 *Charge density distribution on convex surface after applying −3 kV DC voltage for 30 min by the improved algorithm [86]*

are performed both numerically and experimentally. The initial charge density distribution is shown in Fig. 29*a*. The probe scans two times from one side by changing d and g, where d is the distance between the probe and the Polymethylmethacrylate (PMMA) plate; g is the distance between the PMMA plate and the ground electrode. The estimated charge density distribution was calculated based on bilateral surface potential measurements and the results are shown in Fig. 29*b*.

It can be seen that the estimated charge distribution qualitatively coincides with the original one, which verifies the effectiveness of the algorithm. The charge distribution on both surfaces of the insulating plate can be obtained by changing d and g or turn the measured object upside down. Kumada *et al.* compared the precision of the two methods. They found that when the probe scans both surfaces of the insulating plate by changing d and g, the PMSE was 7.1% on the upper surface and 13% on the lower surface. The SNR was 23.0 dB on the upper surface and 17.7 dB on the lower surface. When the probe scans both surfaces by turning the measured object upside down, the PMSE was 6.6% on the upper surface and lower surface. The SNR was 23.6 dB on the upper surface and lower surface. It can be found that the SNR for both methods exceeds 20 dB, and the results when method scans both surfaces by turning the measured object upside down are more accurate.

Our recently published work also emphasises the influence of the surface charge on both sides of the insulator [86]. An improved algorithm based on the measurement of bilateral surface potential was developed. The related algorithm introduces finite element division on both sides of a spacer, where $1 \sim n_1$ are the area on concave surface, $n_1 + 1 \sim n$ are the area on convex surface. Then (45) can be obtained from (18):

$$\begin{bmatrix} P_{11} & P_{12} & \cdots & P_{1n} \\ P_{21} & P_{22} & \cdots & P_{2n} \\ \vdots & \vdots & \ddots & \vdots \\ P_{n_1 1} & P_{n_1 2} & \cdots & P_{n_1 n} \\ P_{n_1+1,1} & P_{n_1+1,2} & \cdots & P_{n_1+1,n} \\ \vdots & \vdots & \ddots & \vdots \\ P_{n1} & P_{n2} & \cdots & P_{nn} \end{bmatrix} \begin{bmatrix} \sigma'_1 \\ \sigma'_2 \\ \vdots \\ \sigma'_{n_1} \\ \sigma'_{n_1+1} \\ \vdots \\ \sigma'_n \end{bmatrix} = \begin{bmatrix} \Phi_1 \\ \Phi_2 \\ \vdots \\ \Phi_{n_1} \\ \Phi_{n_1+1} \\ \vdots \\ \Phi_n \end{bmatrix} \tag{45}$$

The definition of P_{ij} is the same as in (19), and it is noted that the values of r_{ij} obtained for the concave and convex surfaces are different:

$$\begin{bmatrix} F_{11} & F_{12} & \cdots & F_{1n} \\ F_{21} & F_{22} & \cdots & F_{2n} \\ \vdots & \vdots & \ddots & \vdots \\ F_{n_1 1} & F_{n_1 2} & \cdots & F_{n_1 n} \\ F_{n_1+1,1} & F_{n_1+1,2} & \cdots & F_{n_1+1,n} \\ \vdots & \vdots & \ddots & \vdots \\ F_{n1} & F_{n2} & \cdots & F_{nn} \end{bmatrix} \begin{bmatrix} \sigma'_1 \\ \sigma'_2 \\ \vdots \\ \sigma'_{n_1} \\ \sigma'_{n_1+1} \\ \vdots \\ \sigma'_n \end{bmatrix} = \begin{bmatrix} \sigma_1 \\ \sigma_2 \\ \vdots \\ \sigma_{n_1} \\ \sigma_{n_1+1} \\ \vdots \\ \sigma_n \end{bmatrix} \tag{46}$$

The definition of F_{ij} is the same as in (20). Based on TAM described in Section 3.2, the algorithm considers the influence of the surface charge accumulated on both sides of the spacer, which is more accurate than previous algorithms.

Meanwhile, the accuracy of the improved algorithm and the unmodified algorithm was also compared in this work [86]. The DC voltage (−3 kV) was applied to the concave surface of a disc insulator for 30 min. No treatment was performed on the convex surface, and the surface charge density on both sides of the insulator was measured. The results obtained by the two convex algorithms are shown in Figs. 30 and 31.

By comparison, it is found that the amount of negative charge accumulated at the convex side discharge is relatively small, which is due to the fact that the unmodified algorithm does not consider the effects of negative charge on the concave side on the potential measurement on the convex side. Meanwhile, a large amount of positive charges can be found at the undischarged portion as shown in Fig. 30. Since the surface of the insulator before measuring is almost free of surface charge, the untreated part has a small amount of positive charge as shown in Fig. 31, which is more in line with the actual situation. It is proved that for the measurement of the surface charge of the spacer, the improved algorithm considering the measurement of the bilateral surface potential of the insulator has higher accuracy than the traditional algorithm, and the charge density distribution is more consistent with the actual situation.

The inversion algorithm based on bilateral surface potential measurement has high precision and does not require complicated calculation procedures. However, the algorithm is mainly suitable to the translation-invariant systems.

4 Discussions and outlooks

Surface potential measurement and surface charge density calculation provides basis for further exploring mechanisms of the surface charge density and distribution, as well as surface charge-triggered breakdown mechanism. However, until now, we still

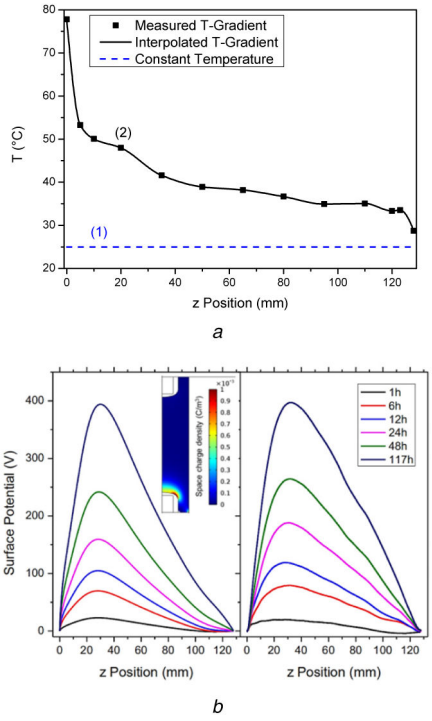

Fig. 32 *Effect of temperature gradient on surface potential measurement*
(a) Experimental temperature measured along the epoxy–gas interface: (1) constant temperature case, (2) temperature-gradient case, ***(b)*** Comparison between (left) simulated and (right) measured surface potential along the epoxy–gas interface with applied DC voltage (−10 kV) [88]

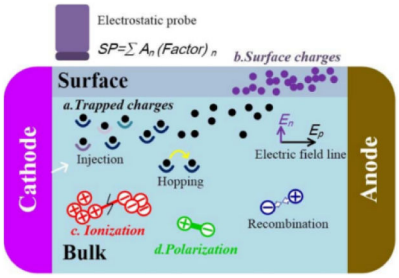

Fig. 33 *Factors within the volume that affect the surface potential measurement [29]*

cannot guarantee any surface charge characterisation technique that is without any drawbacks and these shortcomings in these existing methods inhibit the development of accurate charge measurement technology [9, 31, 87]. In this section, we mainly focus on these drawbacks, and outlooks are also discussed correspondingly.

4.1 Impact of environmental factors

Since the inversion algorithm is based on the electromagnetic field theory, it involves factors such as dielectric constant and conductivity. These factors are affected by environmental factors such as temperature and humidity. However, in the application of existing algorithms for the sake of simplicity the influence of environmental factors is usually ignored, which decreases the accuracy of the calculation results. Our previously published articles have studied the surface potential of the sample with temperature gradient [88]. Temperature distribution along the epoxy–gas interfaces is shown in Fig. 32*a* [89–91]. In accordance with the temperature gradient, most of the space charge is concentrated near the hot electrode, which is shown in Fig. 32*b*.

To improve the accuracy and credibility of the existing algorithms, the measurement of the relationship between environmental factors and dielectric constants, electrical conductivity and other factors can be obtained, and relevant corrections can thereby be made.

4.2 Effect of bulk trapped charges

After applying the DC voltage, a considerable amount of space charges is trapped inside the dielectric [92, 93]. However, these charges can bring potential effects during the surface potential measurement, which would introduce errors in the surface charge detection.

The surface electric potential is the result of the competition between the charge conduction from the volume and the charge conduction from the gas phase [29]. The factor affecting the surface electric potential measurement contains four parts as shown in Fig. 33. Considering the dynamic process of free charges passing through a dielectric, some charges trapped inside the dielectrics and some charges migrate within the dielectric via the hopping conduction mechanism, which these all influence the surface electric field. The charges within the insulator can migrate in the direction of the electric field and eventually accumulate at the interface between the dielectric and the gases. The accumulated surface charges directly affect the detected surface potential.

Meanwhile, to study the effect of bulk trapped charges on the surface potential measurement results, the pulsed electroacoustic (PEA) method was used by many researchers [94, 95]. Chen *et al.* [96] applied a −8 kV DC voltage to the multilayer low density polyethylene (LDPE) film for 2 min by using a needle-plate electrode. Surface potential decay of corona-charged LDPE has been studied using both conventional surface potential measurement and bulk charges measurement (the PEA technique). They concluded that the surface electric charge can inject into the bulk and transport through the interface between two-layer films [96]. Our previous studies also confirmed that the space charge density of the sample can be affected by corona treatment [97]. The accumulated surface charges can be injected into the bulk state, and the decay rate of the surface potential has a strong correlation with corona treatment time duration, which proved the transport of surface charges into bulk traps [97].

4.3 Verification of the accuracy of surface charge inversion algorithms

Currently there are two ways to verify the accuracy of the inversion algorithm:

(a) The Lichtenberg figure method: The surface charge distribution calculated by the inversion algorithm is compared with the Lichtenberg figure. This method can only determine the consistency based on the contour and polarity of the charge distribution, but it cannot quantitatively determine the accuracy of different algorithms.

(b) The numerical simulation method: The initial charge density distribution is set and the initial potential distribution is calculated. The estimated charge distribution is calculated by the inversion algorithms according to the initial potential. The accuracy of the charge estimation is evaluated by defining the SNR and the square root of the PMSE on each surface area by the following equation [85]:

$$\mathrm{SNR} = -10\log_{10}\frac{\sum_{i=1}^{N}\{\hat{\sigma}_i - \sigma_i\}^2}{NA^2} \tag{47}$$

$$\sqrt{\mathrm{PMSE}} = \sqrt{\frac{\sum_{i=1}^{N}\{\hat{\sigma}_i - \sigma_i\}^2}{NA^2}} \tag{48}$$

where A represents the maximum value of $|\sigma_i|$.

4.4 Measurement for real-size GIS/GIL insulator

To study the mechanisms of surface charging phenomena of spacers in real-size GIS, Ootera and Nakanish for the first time performed an experiment on a spacer in a 500 kV DC GIS, in 1988 [21]. The probe was 20 mm away from the spacer surface and seven points (A–G) in the radial direction were selected as the starting points for the measurement as shown in Fig. 34*a*. The

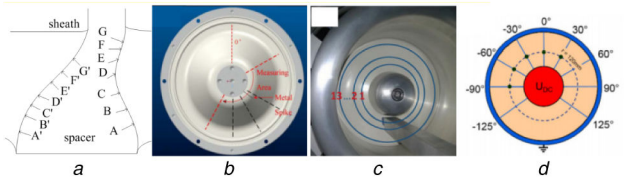

Fig. 34 *Spacer and test sequence on spacer surface*
(a) Real-size 500 kV DC GIS [21], ***(b)*** Real-size ZF-16 220 kV GIS [98], ***(c)*** Real-size 170 kV GIS/GIL [16], ***(d)*** Real-size 320 kV GIS [53]

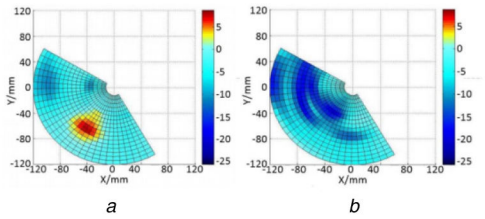

Fig. 35 *Surface charge distribution on the real-size 220 kV GIS spacer under 38 kV DC voltage for 30 and 60 min [98]*
(a) Under 38 kV for 30 min, ***(b)*** Under 38 kV for 60 min

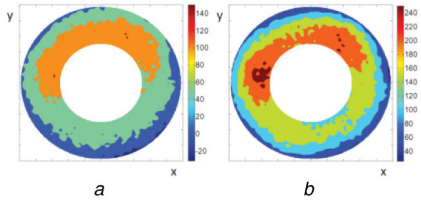

Fig. 36 *Surface potential distribution on the real-size 170 kV GIS/GIL spacer under −170 kV DC voltage for 2 and 4 h [16]*
(a) 2 h, ***(b)*** 4 h

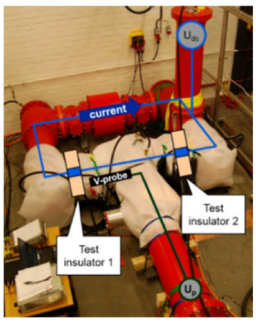

Fig. 37 *Test set-up for the long-term measurement of surface potential on insulator–gas interfaces [53]*

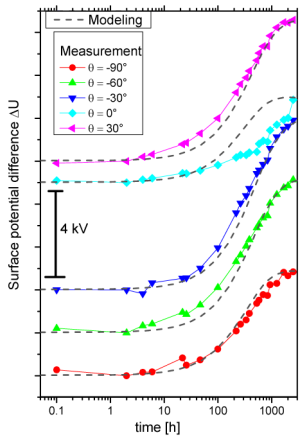

Fig. 38 *Measurement and modelling of surface potential with applied DC voltage 100 kV under 0.45 MPa SF_6 at a relative humidity (RH) of ≤ 8% [53]*

spacer rotated at every 30°; 84 measurement points were made on each surface side. TAM was used to calculate the surface charge density according to the measurement potential. The experimental results are already discussed in Fig. 14. To further study the effect of surface charge accumulation on flashover voltage of real-size GIS insulator, Qi *et al.* [98] performed an experiment on the real ZF-16 220 kV GIS. An arc probe and a bevel probe were used to carry out all-radial and all-angle scanning at the irregular-shaped surface of the spacer. The arc probe structure is discussed in Section 2.2.1. The minimum spatial resolution of charge measurement system was 4.4 mm^2, and the measuring sensitivity of probe can reach 0.0303 $\mu C/(m^2\ mV)$. The measuring area was located from 150° to 300° as shown in Fig. 34*b*. During the measurement, the spacer rotated by every 45° and the probe moved in the radial orientation to measure surface potential of 12 points. The interval between adjacent points on the spacer surface was 1 cm. The time duration between each measurement was controlled within 30 min. TLA was used to calculate the surface charge density according to the measurement potential. The experimental results are shown in Fig. 35. In order to study the influence of local surface roughness of electrodes on the surface charge accumulation, Thanh *et al.* [16] performed an experiment on the real-size 170 kV GIS/GIL spacer using electrodes with different roughness levels. Trek341B was used to measure the surface potential, which has a very large measurement range as shown in Table 1. The probe was 2 mm away from the spacer surface. The probe moved along the 13 rings on the spacer surface as shown in Fig. 34*c*, and the distance between two rings was 2 mm. The time duration of the measurement for the entire surface was within 1 h, and their experimental results are shown in Fig. 36. In our previous research [53–55], the 100 kV DC high voltage was applied to the conductor of a real-size 320 kV DC gas-insulated system (as shown in Fig. 37), and then the voltage was switched off for surface potential measurement. The time duration between disconnecting the system and reconnecting the system was controlled within 2 min so that the error from the charge decay process could be greatly reduced. Trek541A was used to measure the surface potential. The probe was moved following the track as shown in Fig. 34*d*. We indicated that the thermal distribution depends on the azimuthal angle due to natural convection. An exception was the upward direction (0°). In this location, the natural convection is considerably higher than anywhere else, and the associated gas velocity field might interfere with the field-driven ion drift. Therefore, a separate measurement of the temperature distribution should be performed before the measurement.

In addition, we compared the measured surface potential and the simulated results at various azimuthal angles and the results are shown in Fig. 38. The time-scale of the transition to the resistive state (which depends solely on the conductivity of the solid insulation) is well-predicted by the model [53]. This result is essential to derive reliable testing procedure of DC gas-insulated system. Furthermore, the applicability of the model for the prediction of breakdown voltage as a function of DC stress duration is demonstrated.

The differences in surface potential distribution results using simulations and measurements are classified in two categories: (a) experimental determination of conduction parameters in gas and solid [99, 100] and (b) uncertainties/inaccuracy of real-size experiment [101, 102].

Accurate positioning of the surface potential probe is also essential in such a compact environment. To solve the problems regarding inevitable uncertainties in positioning, a self-calibration of the measured radius is achieved by measuring surface potential at the same location with different applied DC voltages (capacitive step method) [103, 104].

4.5 Effect of surface charge on flashover

Surface charge accumulation causes local electric field distortion, which may induce the flashover along the surface. In 1994, it was reported that the low energy flashover on the spacer surface is likely to be related to surface charge accumulation [105]. The

triggering of the flashover is not directly related to the amount of surface charges, since it is found that a small amount of charge can also cause a high local electric field [84]. The presence of hetero-polarity charges is more likely to induce a surface flashover [106]. While recent studies have shown that the homo-polarity charges injected into the volume can result in a potential enhancement near the high voltage electrode, which is equivalent to the extension of the high voltage electrode towards ground electrode, thereby reduces the flashover inception voltage [19]. To further explore surface charge-triggered surface breakdown mechanism, in particular the surface charge density and distribution as well as further estimations of the electric field distortion, more suitable and accurate measurement techniques of surface charge accumulation are still required.

5 Conclusion

As a review while also a reference, this paper reviews the current status, development needs and potential developing orientation of surface charge measurement techniques, including surface potential measurement methods and charge inversion algorithms. Until now, however, there is no effective surface charge distribution measurement method that is suggested since shortcomings in the currently existed methods are able to block in part the development of accurate charge measurement technology and the measurement method is determined by the boundary conditions and specific requirements. Improved algorithms based on the bilateral surface potential measurement and IλFA are more accurate than λFA and φFA algorithms for translation-invariant systems that are generally recognised by researchers. However, these algorithms are not suitable for some complex-shaped insulators in GIS/GIL. TAM is the algorithm commonly used by researchers but its complexity somehow limits its further promotion. λFA and φFA produce a larger error at the boundary conditions which make them difficult to be improved. TLA requires less calculation, however, its limits lies in the affiliated errors and low accuracy compared with other methods. Therefore, an accurate measurement of surface charges is absolutely essential for the design and proper testing of gas-insulated HVDC systems. The cases mentioned in the discussion can be obstacles that inhibit the study of charge-induced flashover mechanisms. More effort should be put into the above-mentioned aspects to develop more precise surface charge measurement techniques.

6 Acknowledgment

This work was supported in part by the National Natural Science Foundation of China (Grant No. 51677113).

7 References

[1] Du, B.X., Li, J.: 'Effects of ambient temperature on surface charge and flashover of heat-shrinkable polymer under polarity reversal voltage', *IEEE Trans. Dielectr. Electr. Insul.*, 2016, **23**, (2), pp. 1190–1197

[2] Lutz, B., Kindersberger, J.: 'Influence of the relative humidity on the DC potential distribution of polymeric cylindrical model insulators'. Proc. IEEE Int. Conf. Condition Monitoring and Diagnosis, Tokyo, Japan, 2010, paper C4-4

[3] Li, C.Y., He, J.L., Hu, J.: 'Surface morphology and electrical characteristics of direct fluorinated epoxy-resin/alumina composite', *IEEE Trans. Dielectr. Electr. Insul.*, 2016, **23**, pp. 3071–3077

[4] Zhang, C., Lin, H.F., Zhang, S., *et al.*: 'Plasma surface treatment to improve surface charge accumulation and dissipation of epoxy resin exposed to DC and nanosecond-pulse voltages', *J. Phys. D: Appl. Phys.*, 2017, **50**, p. 405203

[5] Du, B.X., Du, Q., Li, J., *et al.*: 'Carrier mobility and trap distribution dependent flashover characteristics of epoxy resin', *Gener. Transm. Distrib.*, 2018, **12**, pp. 446–471

[6] Li, C.Y., Hu, J., Lin, C.J., *et al.*: 'Surface charge migration and dc surface flashover of surface-modified epoxy-based insulators', *J. Phys. D: Appl. Phys.*, 2017, **50**, (6), p. 065301

[7] Cooke, C.M.: 'Charging of insulator surfaces by ionization and transport in gases', *IEEE Trans. Dielectr. Electr. Insul.*, 1982, **EI-17**, (2), pp. 172–178

[8] Mazzanti, G., Stomeo, G., Mancini, S.: 'State of the art in insulation of gas insulated substations: main issues, achievements, and trends', *IEEE Electr. Insul. Mag.*, 2016, **32**, (5), pp. 18–31

[9] Wu, Z., Zhang, Q., Ma, J., *et al.*: 'Effectiveness of on-site dielectric test of GIS equipment', *IEEE Trans. Dielectr. Electr. Insul.*, 2018, **25**, (4), pp. 1454–1460

[10] Schueller, M., Straumann, U., Franck, C.M.: 'Role of ion sources for spacer charging in SF6 gas insulated HVDC systems', *IEEE Trans. Dielectr. Electr. Insul.*, 2014, **21**, pp. 352–359

[11] Xue, J., Wang, H., Chen, J., *et al.*: 'Effects of surface roughness on surface charge accumulation characteristics and surface flashover performance of alumina-filled epoxy resin spacers', *J. Appl. Phys.*, 2018, **124**, (8), p. 083302

[12] Li, J., Du, B.X., Liang, H.C., *et al.*: 'Surface functional graded spacer for compact HVDC gaseous insulated system', *IEEE Trans. Dielectr. Electr. Insul.*, 2019, **26**, (2), pp. 664–667

[13] Lutz, B., Kindersberger, J.: 'DC potential distribution of cylindrical polymeric model insulators at different environmental conditions'. ETGFachbericht 125, Isoliersysteme bei Gleich- und Mischfeldbean-spruchung, Berlin, Germany, paper 2.2, 2010

[14] Tenbohlen, S., Schroder, G.: 'The influence of surface charge on lightning impulse breakdown of spacers in SF6', *IEEE Trans. Dielectr. Electr. Insul.*, 2000, **7**, pp. 241–246

[15] Li, C.Y., Lin, C.J., Liu, W.D., *et al.*: 'Novel HVDC spacers by adaptive control of surface charges – part I: charge transport and control strategy', *IEEE Trans. Dielectr. Electr. Insul.*, 2018, **25**, (4), pp. 1238–1247

[16] Vu-Cong, T., Zavattoni, L., Vinson, P., *et al.*: 'Surface charge measurements on epoxy spacer in HVDC GIS/GIL in SF6'. Annual Report Conf. Electrical Insulation and Dielectric Phenomena, Toronto, ON, Canada, 2016, pp. 93–96

[17] Li, C.Y., Lin, C.J., Liu, W.D., *et al.*: 'Novel HVDC spacers by adaptive control of surface charges – part II: experiment', *IEEE Trans. Dielectr. Electr. Insul.*, 2018, **25**, (4), pp. 1248–1258

[18] Liang, H.C., Du, B.X., Li, J., *et al.*: 'Effects of non-linear conductivity on charge trapping and de-trapping behaviours in epoxy/SiC composites under DC stress', *Gener. Transm. Distrib.*, 2018, **12**, pp. 83–89

[19] Li, C.Y., Hu, J., Lin, C.J., *et al.*: 'The neglected culprit of DC surface flashover-electron migration under temperature gradients', *Sci. Rep.*, 2017, **7**, pp. 1–11

[20] Zhou, H.Y., Ma, G.M., Li, C.R., *et al.*: 'Impact of temperature on surface charges accumulation on insulators in SF6-filled DC-GIL', *IEEE Trans. Dielectr. Electr. Insul.*, 2017, **24**, pp. 601–610

[21] Ootera, H., Nakanishi, K.: 'Analytical method for evaluating surface charge distribution on a dielectric from capacitive probe measurement – application to a cone-type spacer in ±500 kV DC-GIS', *IEEE Trans. Power Deliv.*, 1988, **3**, pp. 165–172

[22] Li, C.Y., Lin, C.J., Chen, G., *et al.*: 'Field-dependent charging phenomenon of HVDC spacers based on dominant charge behaviors', *Appl. Phys. Lett.*, 2019, **114**, (20), p. 202904

[23] Zhang, B., Gao, W., Qi, Z., *et al.*: 'Inversion algorithm to calculate charge density on solid dielectric surface based on surface potential measurement', *IEEE Trans. Instrum. Meas.*, 2017, **66**, (12), pp. 3316–3326

[24] Kawasaki, T., Arai, Y., Takada, T.: 'Two-dimensional measurement of electrical surface charge distribution insulating by electro-optic Pockels effect', *Jpn. J. Appl. Phys.*, 1991, **30**, (30), pp. 1262–1265

[25] Lichtenberg, G.C.: 'Nova methodo naturam AC motum fluidi electrici investigandi', *Comment. Soc., Göttingen*, 1778, **8**, pp. 168–179

[26] Murooka, Y., Koyama, S.: 'Nanosecond surface discharge study by using dust figure techniques', *J. Appl. Phys.*, 1973, **44**, (4), pp. 1576–1580

[27] Murooka, Y., Takada, T., Hiddaka, K.: 'Nanosecond surface discharge and charge density evaluation part I: review and experiments', *IEEE Electr. Insul. Mag.*, 2001, **17**, (2), pp. 6–16

[28] Okabe, S., Kumada, A.: 'Measurement methods of accumulated electric charges on spacer in gas insulated switchgear', *IEEE Trans. Power Deliv.*, 2007, **22**, (3), pp. 1547–1556

[29] Li, C.Y., Lin, C.J., Zhang, B., *et al.*: 'Understanding surface charge accumulation and surface flashover on spacers in compressed gas insulation', *IEEE Trans. Dielectr. Electr. Insul.*, 2018, **25**, (4), pp. 1152–1166

[30] Li, C.Y., Zhu, Y.J., He, J.L., *et al.*: 'Donut-shaped charge cluster triggers unpredictable surface flashover in HVDC spacers', preparing

[31] Zhang, J.W., Cao, D.K., Diaham, S., *et al.*: 'Research on potential induced degradation (PID) of polymeric backsheet in PV modules after salt-mist exposure', *Sol. Energy*, 2019, **188**, pp. 475–482

[32] Zhang, Z.S., Deng, B.J., Li, C.Y., *et al.*: 'Multiphysics coupled modelling in HVDC GILs: critical re-examination of ion mobility selection', *IEEE Trans. Dielectr. Electr. Insul.*, 2019, **26**, (3), pp. 835–842

[33] Yan, W., Li, C.Y., Lei, Z.P., *et al.*: 'Surface charging on HVDC spacers considering time-varying effect of temperature and electric fields', *IEEE Trans. Dielectr. Electr. Insul.*, 2019, **26**, (4), pp. 1316–1324

[34] Davies, D.K.: 'Examination of the electrical properties of insulators by surface charge measurement', *J. Sci. Instrum.*, 1967, **44**, (7), pp. 521–524

[35] Wang, F., Qiu, Y.C., Pfeiffer, W., *et al.*: 'Insulator surface charge accumulation under impulse voltage', *IEEE Trans. Dielectr. Electr. Insul.*, 2004, **11**, (5), pp. 847–854

[36] Zhang, Y.L., Wang, F., Li, Z., *et al.*: 'Development of surface charge detection device for DC composite insulator', *High Volt. Eng.*, 2014, **40**, (5), pp. 1514–1519 (in Chinese)

[37] Qi, B., Gao, C.J., Xing, Z.L., *et al.*: 'Distribution characteristic for surface charge on GIS insulator under DC/AC voltage', *Proc. CSEE*, 2016, **36**, (21), pp. 5990–6001 (in Chinese)

[38] Wang, F., Zhang, Q., Qiu, Y.C., *et al.*: 'Insulator surface charge accumulation under DC voltage'. Proc. Conf. Record 2002 IEEE Int. Symp. Electr. Insul. (Cat No. 02CH37316), Boston, MA, USA, 7–10 April 2002

[39] Wang, F., Liu, H.B.: 'Study on on-line monitoring of surface charge of insulator based on generalized probe', *Transducer Microsyst. Technol.*, 2011, **30**, (8), pp. 59–61 (in Chinese)

[40] Zhuang, Y., Chen, G., Rotaru, M.: 'Charge injection in gold ground electrode corona charged polyethylene film: surface potential decay and corona charging current measurement'. Proc. 2011 – 14th Int. Symp. Electrets, Montpellier, France, 28–31 August 2011

[41] Molini, P., Agnel, S., Castellon, J.: 'Investigations on charge accumulation and relaxation in polycrystalline Al_2O_3: correlations of surface potential measurements with other techniques'. Proc. 2010 10th IEEE Int. Conf. Solid Dielectr., Potsdam, Germany, 4–9 July 2010

[42] Sam, Y.L., Lewin, P.L., Davies, A.E., *et al.*: 'Dynamic measurement of surface charge'. Proc. 2000 Eighth Int. Conf. Dielectr. Mater., Meas. Appl. (IEE Conf. Publ. No. 473), Edinburgh, UK, 17–21 September 2000

[43] Xue, J.Y., Wang, H., Liu, Y., *et al.*: 'Surface charge distribution patterns of a truncated cone-type spacer for high-voltage direct current gas-insulated metal-enclosed transmission line/gas-insulated metal-enclosed switchgear', *IET Sci. Meas. Technol.*, 2018, **12**, (4), pp. 436–442

[44] Du, B.X., Chang, R., Zhu, W.B., *et al.*: 'Temperature-dependent surface charge and discharge behaviour of converter transformer oil–paper insulation under DC voltage', *IET Sci. Meas. Technol.*, 2019, **13**, (1), pp. 29–34

[45] Pan, C., Song, W.B., Tang, J., *et al.*: 'Influence of surface charge decay on cavity PD frequency at DC voltage', *IET Sci. Meas. Technol.*, 2019, **13**, (2), pp. 193–200

[46] Li, C.Y., Hu, J., Lin, C.J., *et al.*: 'The control mechanism of surface traps on surface charge behavior in alumina-filled epoxy composites', *J. Phys. D: Appl. Phys.*, 2016, **49**, p. 445304

[47] Rossi, F., Opat, G.I., Cimmino, A.: 'Modified Kelvin technique for measuring strain-induced contact potentials', *Rev. Sci. Instrum.*, 1992, **63**, (7), pp. 3736–3743

[48] Schueller, M., Gremaud, R., Baur, M., *et al.*: 'Kelvin probe for surface potential measurements on epoxy insulators for HVDC applications'. Proc. 2018 IEEE Int. Conf. High Volt. Eng. Appl. (ICHVE), Athens, Greece, 10–13 September 2018

[49] Fatihou, A., Dascalescu, L., Zouzou, N., *et al.*: 'Measurement of surface potential of non-uniformly charged insulating materials using a non-contact electrostatic voltmeter', *IEEE Trans. Dielectr. Electr. Insul.*, 2016, **23**, (4), pp. 2377–2384

[50] Kindersberger, J., Lederle, C.: 'Surface charge decay on insulators in air and sulfurhexafluorid – part II: measurements', *IEEE Trans. Dielectr. Electr. Insul.*, 2008, **15**, (4), pp. 949–957

[51] Tschentscher, M., Franck, C.M.: 'Conduction processes in gas-insulated HVDC equipment: from saturated ion currents to micro-discharges', *IEEE Trans. Dielectr. Electr. Insul.*, 2018, **25**, (4), pp. 1167–1176

[52] Tschentscher, M., Franck, C.M.: 'Microscopic charge provision at interfaces of gas-insulated (HVDC/HVAC) systems', *IEEE Trans. Dielectr. Electr. Insul.*, 2018, **25**, (4), pp. 1186–1194

[53] Gremaud, R., Doiron, C., Baur, M., *et al.*: 'Solid-gas insulation in HVDC gas-insulated system: measurement, modeling and experimental validation for reliable operation'. CIGRÉ Report D1-101, 46th CIGRÉ Session, Palais des Congrès de Paris, Paris, France, 21–26 August 2016

[54] Gremaud, R., Doiron, C., Baur, M., *et al.*: 'Solid-gas insulation in HVDC gas-insulated system: measurement, modeling and experimental validation for reliable operation', *CIGRÉ Sci. Eng.*, 2017, **7**, pp. 133–142, 'Best of' Paris Session 2016, CIGRE © 21, rue d'Artois, 75008 Paris; ISSN: 1286-1146

[55] Riechert, U.: 'Verification of HVDC GIS spacer models'. CIGRÉ Contribution D1, PS1-Q1, 47th CIGRÉ Session, Palais des Congrès de Paris, Paris, France, 26–31 August 2018

[56] Wang, Q., Zhang, G., Wang, X.: 'Characteristics and mechanisms of surface charge accumulation on a cone-type insulator under dc voltage', *IEEE Trans. Dielectr. Electr. Insul.*, 2012, **19**, (1), pp. 150–155

[57] Faircloth, D.C., Allen, N.L.: 'High resolution measurements of surface charge densities on insulator surfaces', *IEEE Trans. Dielectr. Electr. Insul.*, 2003, **10**, (2), pp. 285–290

[58] Kumada, A., Okabe, S., Hidaka, K.: 'Resolution and signal processing technique of surface charge density measurement with electrostatic probe', *IEEE Trans. Dielectr. Electr. Insul.*, 2004, **11**, (1), pp. 122–129

[59] Ma, G.M., Zhou, H.Y., Liu, S.P., *et al.*: 'Measurement and simulation of charge accumulation on a disc spacer with electro-thermal stress in SF6 gas', *IEEE Trans. Dielectr. Electr. Insul.*, 2018, **25**, (4), pp. 1221–1229

[60] Naik, M.G.C., Amarnath, J., Kamakshiah, S.S.: 'A new optimised design of single phase gas insulated cone type insulator', *Int. J. Eng. Sci. Technol.*, 2012, **4**, (3), pp. 929–936

[61] Lang, S.B., Das-gupta, D.K.: 'Laser intensity modulation method: A technique for determination of spatial distributions of polarization and space charge in polymer electrets'. Proc. 5th Int. Symp. Eletrets, Heidelberg, 1985, pp. 444–449

[62] Winte, A., Kindersberger, J.: 'Surface charge density distributions on insulating plates under pressurized gases'. 12th Int. Symp. High Volt. Eng., Bangalore, 2001, vol. 1, pp. 24–28

[63] Specht, H.: 'Oberflächcnladungen bei rotatians symmetrischen isolierstoffkörpern', *ETZ-A*, 1976, **97**, p. 474

[64] Pedersen, A.: 'On the electrostatic field near the charged surface of an insulator with special reference to surface charge probe measurements'. Gaseous Dielectrics IV, Knoxville, TN, USA, 1984, pp. 414–420

[65] Wintle, H.J.: 'Theory of the potential probe used in static electrification measurements on insulators', *Phys. E*, 1970, **3**, pp. 334–336

[66] Khalil, M.S., Hansen, B.S.: 'Investigation of space charge in low-density polyethylene using a field probe technique', *IEEE Trans. Electr. Insul.*, 1988, **23**, pp. 441–445

[67] Lin, C.J., Li, C.Y., Zhang, G.X., *et al.*: 'Review and prospect of surface charge inversion algorithm of cone-type spacer based on surface potential measurement', *Proc. CSEE*, 2016, **36**, (24), pp. 6654–6663 (in Chinese)

[68] Zheng, N., Huang, X., Yu, K., *et al.*: 'Measurement of surface charge distribution on insulating material under pulsed voltage'. Proc. of the 24th ISDEIV 2010, Braunschweig, Germany, 30 August–3 September 2010

[69] Gao, C.J., Qi, B., Xing, Z.L., *et al.*: 'Development of a surface charge measurement system for GIS insulator in SF6'. Proc. 2015 IEEE Conf. Electr. Insul. Dielectr. Phenom. (CEIDP), Ann Arbor, MI, USA, 18–21 October 2015

[70] Takuma, T., Yashima, M., Kawamoto, T.: 'Principle of surface charge measurement for thick insulating specimens', *IEEE Trans. Dielectr. Electr. Insul.*, 1988, **5**, (4), pp. 497–504

[71] Yashima, M., Fujinami, H., Takuma, T.: 'Measurement of accumulated charge on dielectric surfaces with an electrostatic probe'. Proc. 5th Int. Symp. Gaseous Dielectr. V, Knoxville, TN, USA, 1987, pp. 242–248

[72] Ahmed, N.H., Srinivas, N.N.: 'Review on space charge measurements in dielectrics', *IEEE Trans. Dielectr. Electr. Insul.*, 1997, **4**, pp. 644–656

[73] Pedersen, A.: 'On the electrostatics of probe measurements of surface charge densities'. Proc. Fifth Int. Symp. Gaseous Dielectr. V, Knoxville, TN, USA, 1987, pp. 235–241

[74] Rerup, T.O., Crichton, G.C., McAllister, I.W.: 'Using the λ function to evaluate probe measurements of charged dielectric surfaces', *IEEE Trans. Dielectr. Electr. Insul.*, 1996, **3**, (6), pp. 770–777

[75] Reruo, T.O., Crichton, G.C., McAllister, I.W.: 'The response of electrostatic probes via the λ-function'. Conf. Record 1994 IEEE Int. Symp. Electr. Insul., Pittsburgh, PA, USA, 1994

[76] Okabe, S., Okada, T., Yuasa, S., *et al.*: 'Effect of DC pre-stress on dielectric characteristics of an insulator in SF6 gas'. Proc. 12th Int. Symp. High Volt. Eng., Bangalore, 2001, vol. 2, pp. 351–354

[77] Kumada, A., Okabe, S., Hidaka, K.: 'Influences of probe geometry and experimental errors on spatial resolution of surface charge measurement with electrostatic probe', *IEEE Trans. Dielectr. Electr. Insul.*, 2005, **12**, (6), pp. 1172–1181

[78] Zhang, B., Qi, Z., Gao, W., *et al.*: 'Accumulation characteristics of surface charge on a cone-type model insulator under DC voltage'. Proc. 2018 IEEE Int. Conf. High Volt. Eng. Appl. (ICHVE), Athens, Greece, 10–13 September 2018

[79] Xue, J.Y., Chen, J.H., Dong, J.H., *et al.*: 'The regulation mechanism of Sic/epoxy coatings on surface charge behavior and flashover performance of epoxy/alumina spacers', *J. Phys. D: Appl. Phys.*, 2019, **52**, article number: 405502

[80] Park, S.C., Park, M.K., Kang, M.G.: 'Super-resolution image reconstruction: A technical overview', *IEEE Signal Process. Mag.*, 2003, **20**, pp. 21–36

[81] Johansson, T., Crichton, G.C., McAllister, I.W.: 'Influence of probe geometry on the response of an electrostatic probe'. IEEE Conf. Electr. Insul. Dielectr. Phenom. (CEIDP), Austin, 1999, pp. 137–141

[82] Kumada, A., Okabe, S., Hidaka, K.: 'Charge accumulation on truncated cone spacer under dc electric field', *IEEE Trans. Dielectr. Electr. Insul.*, 2004, **11**, pp. 929–938

[83] Winter, A., Kindersberger, J.: 'Measurement of double layer surface charge density distributions on insulating plates with capacitive probes'. Proc. Intern. Conf. Adv. Process, Test. Appl. Dielectr. Mater., Wroclaw, Poland, 2001, pp. 123–128

[84] Winter, A., Kindersberger, J.: 'Surface charge accumulation on insulating plates in SF6 and the effect on DC and AC break-down voltage of electrode arrangements'. IEEE Conf. Electr. Insul. Dielectr. Phenom., Cancun, Mexico, 2002, pp. 454–461

[85] Kumada, A., Okabe, S.: 'Measurement of surface charge on opposite sides of a planar insulator using an electrostatic probe', *IEEE Trans. Dielectr. Electr. Insul.*, 2004, **11**, (6), pp. 919–928

[86] Lin, C.J., Li, C.Y., He, J.L., *et al.*: 'Surface charge inversion algorithm based on bilateral surface potential measurements of cone-type spacer', *IEEE Trans. Dielectr. Electr. Insul.*, 2017, **24**, (3), pp. 1905–1912

[87] Li, C.Y., Xu, Y., Lin, C.J., *et al.*: 'Surface charging phenomenon on HVDC spacers in compressed SF6 insulation and charge tailoring strategies', CSEE-JPES, accepted

[88] Gremaud, R., Schueller, M., Doiron, C.B., *et al.*: 'Experimental validation of electric field modeling in DC gas-insulated system'. International Study Committee Meeting and Colloquium 2015 CIGRÉ Study Committee D1 (Materials and Emerging Test Techniques, Trends in Technology, Materials, Testing and Diagnostics Applied to Electric Power Systems, Proceedings, paper 21), Rio de Janeiro, Brazil, 13th–18th September 2015

[89] Schueller, M.: 'Role and impact of different charge sources on surface charge accumulation in gas insulated HVDC systems'. PhD, High Voltage Laboratory, ETHZ, Zürich, 2014, doi: http://dx.doi.org/10.3929/ethz-a-010388684

[90] Hering, M., Gremaud, R., Speck, J., *et al.*: 'Flashover behaviour of insulators with inhomogeneous temperature distribution in gas insulated systems under DC voltage stress'. Int. Conf. High Volt. Eng. Appl., Poznan, Poland, 2014

[91] Schueller, M., Gremaud, R., Franck, C.M.: 'Accuracy of surface potential measurements of HVDC spacers'. Int. Conf. High Volt. Eng. Appl., Poznan, Poland, 2014

[92] Kikuchi, S., Mizutani, S., Miyake, H., *et al.*: 'Effect of heat treatment on space charge accumulation in epoxy resin under high DC stress'. IEEE Conf. Electr. Insul. Dielectr. Phenom., Des Moines, IA, USA, 2014, pp. 808–811

[93] Dong, J.H., Wu, K., Shao, Z.H., *et al.*: 'Space charge accumulation in epoxy resin and its nanocomposites under temperature gradient'. IEEE Conf. Electr. Insul. Dielectr. Phenom., Ann Arbor, MI, USA, 2015

[94] Fukuma, M., Maeno, T., Fukunaga, K.: 'Cross-section space charge measurement system'. IEEE Int. Conf. Solid Dielectr., Toulouse, France, 2004, pp. 182–185

[95] Fukuma, M., Masuda, N., Fukunaga, K.: 'Development of sensor scanning type space charge measurement system'. Annual Report Conf. Electr. Insul. Dielectr. Phenom. (CEIDP), West Lafayette, IN, USA, 2010, pp. 1–4

[96] Xu, Z., Zhang, L., Chen, G.: 'Decay of electric charge on corona charged polyethylene', *J. Phys. D: Appl. Phys.*, 2007, **40**, (22), pp. 7085–7089

[97] Lei, Z., Li, C., Men, R., *et al.*: 'Mechanism of bulk charging behavior of ethylene propylene rubber subjected to surface charge accumulation', *J. Appl. Phys.*, 2018, **124**, (24), article number: 244103
[98] Qi, B., Gao, C.J., Li, C.R., *et al.*: 'Effect of surface charge accumulation on flashover voltage of GIS insulator in SF6 under DC and AC voltages'. Annu. Rep. Conf. Electr. Insul. Dielectr. Phenom., Ann Arbor, MI, USA, 2015, pp. 18–21
[99] Gremaud, R., Zhao, Z., Baur, M.: 'Measurement of DC conduction in alumina-filled epoxy'. 1st Int. Conf. Dielectr. (ICD), Montpellier, France, 2016
[100] Simka, P., Teppati, V., Vukas, M.: 'Charge injection and multiplication in SF6 and vacuum under DC electric fields'. ICPADM 2015, Sydney, Australia, 2015
[101] Zavattoni, L.: 'Conduction phenomena through gas and insulating solids in HVDC Gas Insulated Substations, and consequences on electric field distribution'. PhD, Université de Grenoble, Grenoble, 2015
[102] Zavattoni, L., Hanna, R., Lesaint, O.: 'Dark current measurements in humid SF_6: influence of electrode roughness, relative humidity and pressure', *J. Phys. D: Appl. Phys.*, 2015, **48**, p. 375501
[103] Kaufmann, B., Kudoke, M., Großmann, S.: 'Experimental verification of convective heat transfer computations for gas insulated switchgear'. 2013 4th Int. Youth Conf. Energy (IYCE), Siofok, Hungary, 2013, pp. 1–6
[104] Riechert, U., Straumann, U., Gremaud, R.: 'Compact gas-insulated systems for high voltage direct current transmission: basic design'. Presented at the IEEE Transmission and Distribution Conference and Exposition, Dallas, USA, 2016
[105] Wang, C.: 'Physical model for surface charge supported flashover'. Gaseous Dielectrics VII, Knoxville, TN, USA, 1994, pp. 519–525
[106] Kumara, S., Alam, S., Hoque, I.R., *et al.*: 'DC flashover characteristics of a polymeric insulator in presence of surface charges', *IEEE Trans. Dielectr. Electr. Insul.*, 2012, **19**, pp. 1084–1090